

Article

Investigation of the Deformation Mechanism of a near β Titanium Alloy through Isothermal Compression

Jie Wu ¹, Zhidan Lü ¹, Changjiang Zhang ^{1,*}, Jianchao Han ², Hongzhou Zhang ³, Shuzhi Zhang ¹ , Muhammad Hayat ³ and Peng Cao ^{3,*} 

¹ School of Materials Science and Engineering, Taiyuan University of Technology, Taiyuan 030024, China; zdlv@126.com (J.W.); zdlv_tyut@163.com (Z.L.); zhshzh1984@163.com (S.Z.)

² School of Mechanical Engineering, Taiyuan University of Technology, Taiyuan 030024, China; hanjianchao@tyut.edu.cn

³ Department of Chemical and Materials Engineering, University of Auckland, Private Bag 92019, Auckland 1142, New Zealand; hongzhou1229@gmail.com (H.Z.); mhay097@aucklanduni.ac.nz (M.H.)

* Correspondence: zhangchangjiang@tyut.edu.cn (C.Z.); p.cao@auckland.ac.nz (P.C.); Tel.: +86-351-6010-022 (C.Z.); +64-9-923-6924 (P.C.)

Received: 17 October 2017; Accepted: 7 November 2017; Published: 12 November 2017

Abstract: This study investigated the hot deformation behavior of Ti-4Al-1Sn-2Zr-5Mo-8V-2.5Cr alloy through isothermal compression tests at temperatures from 780 to 930 °C with strain rates ranging from 0.001 to 1 s⁻¹. The flow stress decreases with a decreased strain rate and an increased temperature. A constitutive equation was established for this alloy and the dependence of activation energy on temperature and strain rate is discussed. We further proposed a processing map using the dynamic materials model. On the processing map various domains of flow stability and flow instability can be identified. The deformation mechanisms associated with flow stability regions are mainly dynamic recrystallization (DRX) and dynamic recovery (DRV). The flow instability is manifested in the form of the band of flow localizations. The optimum processing conditions are suggested such that the temperature range is from 780 to 880 °C and the strain rate ranges from 0.001 to 0.01 s⁻¹.

Keywords: isothermal compression; true strain-stress curves; constitutive equation; processing map

1. Introduction

Over the past few decades, many industries have witnessed significantly increasing applications of titanium alloys including in the aerospace, automotive, medical, sports and consumer goods industries [1–3]. Among these titanium materials, beta alloys have been receiving intense interest in aerospace sector due to their high yield strength, good ductility, good fatigue and crack resistances [4,5]. For example, the first commercial β Ti alloy, Ti-13V-11Cr-3Al was used in the Lockheed SR-71 ‘Blackbird’ reconnaissance airplane. Another β Ti alloy Ti-1023 (composition: Ti-10V-2Fe-3Al in wt. %) has also been used in landing gear in Boeing 777 [6]. It is well known that hot working is a critical processing route in the manufacture of β titanium products [7,8]. However, it is also noted that, these alloys are sensitive to the processing conditions such that subtle variations in either temperature or strain rate would result in a significant change in the alloys’ properties. The selection of proper hot working parameters is complex for β titanium in comparison to other structural materials such as aluminum and steel [9]. Additionally, the near-beta forging is also widely used for titanium alloys because excellent properties can be obtained [10,11]. Hence, it is crucial to gain a thorough understanding of how the processing variables affect the deformation characteristics of the β or near β Ti alloys in order to optimize the processing parameters and microstructures.

High temperature compression tests are a common technique to investigate the microstructural evolution of a work-piece via thermo-mechanical treatments [12,13]. Very recently, Zhao et al. [14] investigated the hot deformation behavior of a metastable Ti-1023 Ti alloy. Their experimental results matched well with a constitutive model based on dislocation density theory and dynamic recrystallization kinetics. Another metastable β Ti alloy Ti-1300 has also been extensively investigated. For example, Zhao et al. [15] constructed a processing map and identified two stable deformation regions that are considered suitable for hot processing. Li et al. [16] studied a powder metallurgical titanium aluminide Ti-45Al-7Nb-0.3W (at. %) and correlated the deformation mechanisms with the so-called Zener-Holloman or Z parameter.

In the past years, processing maps have become a standard graphic tool for optimizing materials workability and/or analyzing practical problems for a wide range of materials including metals, composites and intermetallics. In particular, optimal hot workability temperature range and strain rate range can be readily read off on its specific processing map. For instance, the optimal hot processing conditions for a cast TC21 titanium alloy was found to be at temperatures of 1000 to 1150 °C and with strain rates of 0.01 to 0.5 s⁻¹ through the establishment of the processing map [17]. Li et al. [18] also identified a suitable temperature range (from 770 to 850 °C) and strain rate range (from 0.01 to 0.1 s⁻¹) through construction of the processing map for TC17 alloy. In another study, Liu et al. [19] suggested a temperature window of 300 to 350 °C and a strain rate range of 0.001 to 0.1 s⁻¹ for Mg-3Zn-0.8Zr/1HA composite.

The model material in this study, Ti-4Al-1Sn-2Zr-5Mo-8V-2.5Cr alloy, is a newly developed near β titanium alloy for aerospace applications. Few studies are available for this alloy, particularly in relation to the hot deformation behavior. Hence, this work intends to characterize its high temperature deformation behavior and establish a processing map for this particular alloy. This study will provide scientific evidence and contribute to the full implementation of the alloy in aerospace applications.

2. Materials and Methods

The samples for thermo-mechanical testing were obtained from a cast Ti-4Al-1Sn-2Zr-5Mo-8V-2.5Cr ingot, which was melted in an induction skull melting furnace. The chemical compositions are listed in Table 1. The β transus of this alloy was estimated to be 800 °C, measured by a metallographic method.

Table 1. Nominal and actual chemical compositions.

Element	Al	Sn	Zr	Mo	V	Cr	Ti
Nominal wt. %	4.00	1.00	2.00	5.00	8.00	2.50	bal.
Actual wt. %	4.30	1.03	2.07	4.99	8.00	2.50	bal.

Cylindrical specimens 8 mm in diameter and 12 mm high were cut from the ingot. The compression tests were conducted on a Gleeble-3800 thermal-mechanical simulator (Data Sciences International, Minnesota, MN, USA) at a temperature ranging from 780 °C to 930 °C at a temperature interval of 50 °C. The strain rate was 0.001 s⁻¹, 0.01 s⁻¹, 0.1 s⁻¹ and 1 s⁻¹ respectively. The specimens were held for 10 min at the deformation temperature and compressed in a vacuum chamber. The height reduction ratio was 75% for all specimens. After reaching the height reduction, the specimens were held for 2 min to ensure completion of deformation and then immediately quenched in to water to preserve the deformed microstructure. Two pieces of thin tantalum sheets were used to minimize friction and maintain uniform deformation. Central regions of the deformed specimens were sectioned for metallographic examinations by Leica DM2500M optical microscopy (OM) (Leica, Wetzlar, Germany) and Tescan MIRA3LMH scanning electron microscopy (SEM) (Tescan, Brno, Czech Republic). The metallographic samples were polished sequentially with 360–2500 grit SiC paper, followed by electrolytic polishing. Further, the modified Kroll's reagent (3 mL HF + 5 mL HNO₃ + 92 mL H₂O) was used to reveal the microstructures.

3. Results and Discussion

3.1. True Stress-True Strain Curves

Figure 1 presents the true stress-strain curves of the Ti-4Al-1Sn-2Zr-5Mo-8V-2.5Cr alloy at various temperatures and strain rates. As expected, the flow stress is largely dependent on temperature, strain rate and strain rate. At the initial compression stage, the flow stress under all conditions increases rapidly and reaches a peak value when the strain approaches 0.1. This is typical of work hardening. Beyond 0.1 strain, all specimens demonstrate flow softening. In addition, the flow softening becomes more prominent at higher strain rates and lower temperatures. This elevated flow softening is attributed to the adiabatic heating, local temperature rise or flow instability according to some previous studies [20]. It is also clear that, at a given strain rate, the peak flow stress decreases with increasing deformation temperature, a result arising from thermally-assisted dislocation movements. Meanwhile, at a given temperature, the peak value of flow stress increases with increasing strain rate. It is also noted that, at a given temperature, the steady-state flow is much earlier approached at a lower strain rate (e.g., Figure 1a). As shown in Figure 1d, at 930 °C and strain rates $< 0.1 \text{ s}^{-1}$, the steady-state flow stress is almost instantaneously reached.

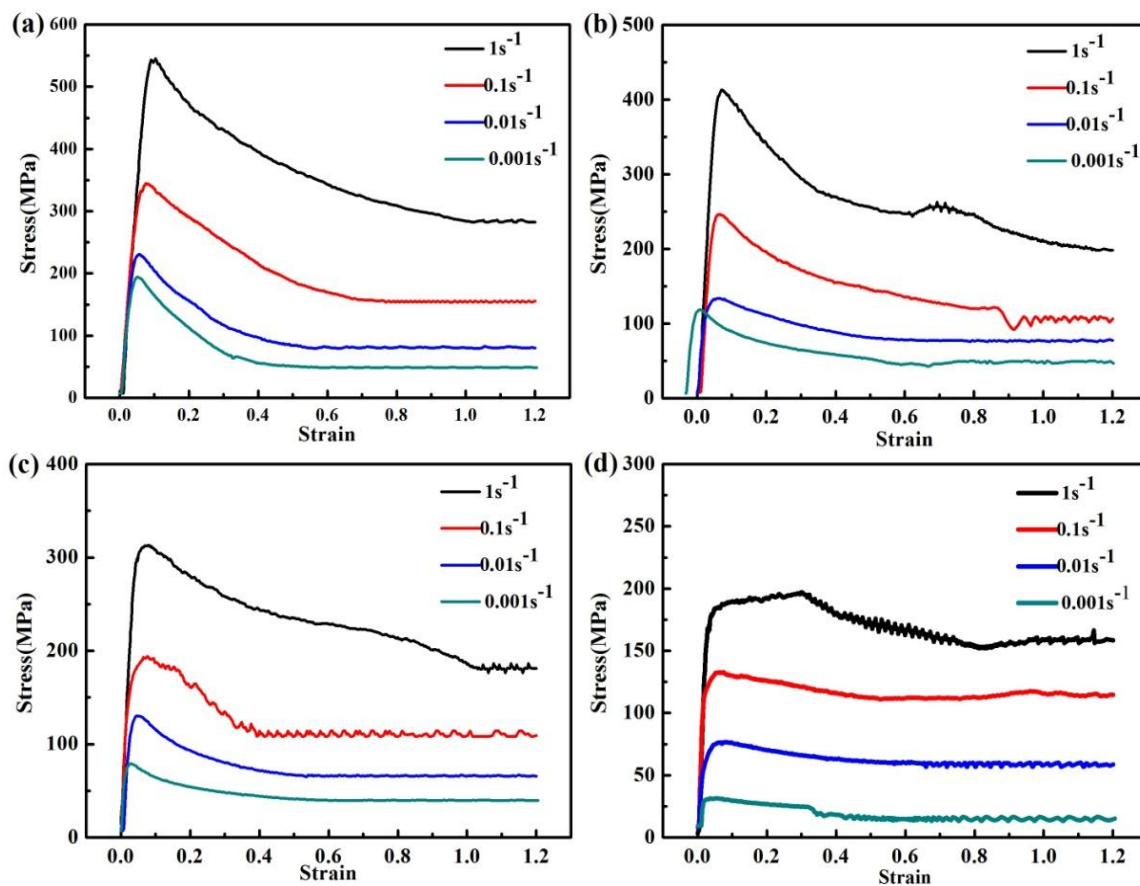


Figure 1. True stress-true strain curves of Ti-4Al-1Sn-2Zr-5Mo-8V-2.5Cr alloy at (a) 780 °C, (b) 830 °C, (c) 880 °C and (d) 930 °C.

The peak flow stress in hot deformation is influenced by strain rate and temperature, as per a hyperbolic-sine Equation (1) [19].

$$\dot{\varepsilon} = A[\sinh(\alpha\sigma)]^n \exp(-Q/RT) \quad (1)$$

where A , α , n are materials constants, R is the molar gas constant, σ is the flow stress, T is absolute temperature and Q is the activation energy for hot deformation.

To model the constitutive equation for the hot deformation of the Ti-4Al-1Sn-2Zr-5Mo-8V-2.5Cr alloy, the values of A , α and n were determined using the experimental data and regression analysis.

Equation (1) can be re-written as

$$Q = R \left. \frac{\partial \ln\{\sinh(\alpha\sigma)\}}{\partial(1/T)} \right|_{\dot{\epsilon}} \cdot \left. \frac{\partial \ln \dot{\epsilon}}{\partial \ln\{\sinh(\alpha\sigma)\}} \right|_T = Rn_1n \quad (2)$$

where $n_1 = \left. \frac{\partial \ln\{\sinh(\alpha\sigma)\}}{\partial(1/T)} \right|_{\dot{\epsilon}}$ is the strain rate sensitivity coefficient and $n = \left. \frac{\partial \ln \dot{\epsilon}}{\partial \ln\{\sinh(\alpha\sigma)\}} \right|_T$ is the temperature sensitivity coefficient. Equation (1) can also be expressed as:

$$\ln \dot{\epsilon} = n \ln[\sinh(\alpha\sigma)] + \ln A - Q/RT \quad (3)$$

A plot of $\ln \dot{\epsilon}$ vs. $\ln[\sinh(\alpha\sigma)]$ for different temperatures is shown in Figure 2a. The inverse of the slope gives the temperature sensitivity coefficient n in Equation (2). Figure 2b shows the relationship of $\ln[\sinh(\alpha\sigma)]$ vs. T^{-1} for different strain rates and their linear regression results. The inverse of the slope gives the strain rate sensitivity coefficient n_1 in Equation (2).

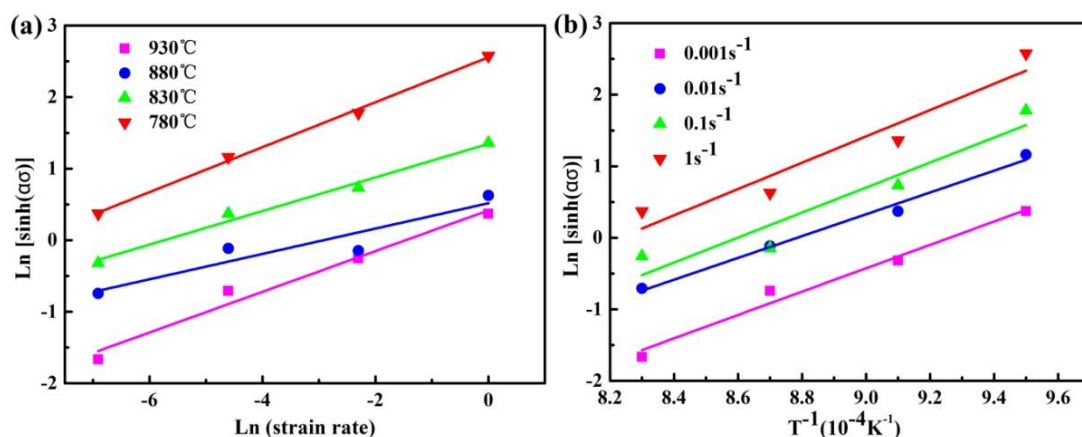


Figure 2. Plots of (a) $\ln[\sinh(\alpha\sigma)]$ vs. $\ln(\text{strain rate})$ and (b) $\ln[\sinh(\alpha\sigma)]$ vs. T^{-1} .

Derived from Figure 2, the variation of Q under various conditions is presented in Figure 3. It can be seen that, at a given temperature, the value of Q changes insignificantly with strain rate. In contrast, for a given strain rate, Q increases sharply when the temperature rises from 780 °C to 830 °C. The rapid change of Q with respect to temperature may be attributed to the phase transformation at approximately 800 °C. It was reported that the globularization, elongation and rotation of α phase may lead to a rapid increase in activation energy [20]. When the temperature further increases, the value of Q decreases. When deformed in the single β field, an increased internal energy arising from increasing temperature leads to a decreased activation energy. These results are consistent with other reports [21]. It is noted that these Q values are much higher than self-diffusion activation energy for either β titanium (153 kJ/mol) or α titanium (169 kJ/mol) [22].

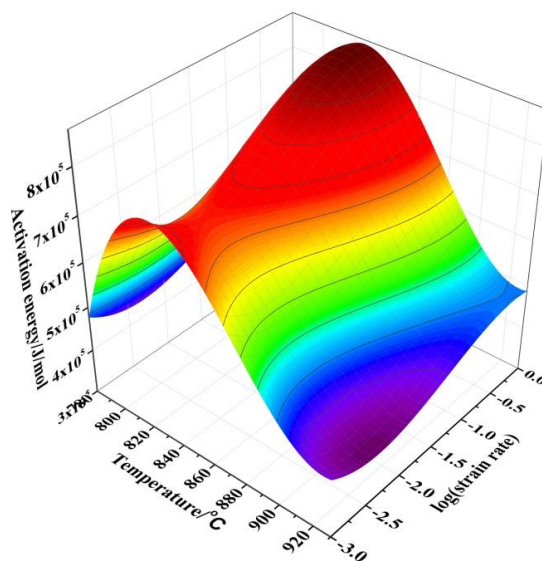


Figure 3. Values of activation energy under various conditions.

The well-known Zener-Hollomon, or Z, parameter is usually used to describe the flow behavior that is a thermally activated process and is expressed as [23]:

$$Z = \dot{\epsilon} \exp \frac{Q}{RT} = A \{ \sinh(\alpha\sigma) \}^n \tag{4}$$

A plot of $\ln(Z)$ versus $\ln[\sinh(\alpha\sigma)]$ is shown in Figure 4. A good linear correlation is seen between the flow stress and the Z value with a regression coefficient R^2 of 0.96. The slope of the plots give a stress exponent value of 3.92, which is close to the corresponding value obtained from Figure 2a. Based on the results obtained, we chose an apparent activation energy of 592 kJ/mol for our alloy. Additionally, the calculated α , n , Q values of some near-beta titanium alloys are listed in Table 2. A constitutive equation of the peak flow stress for our alloy is described as:

$$\sigma = 166.67 \ln \left\{ \left(\frac{Z}{e^{58.58}} \right)^{1/3.92} + \left[\left(\frac{Z}{e^{58.58}} \right)^{2/3.92} + 1 \right]^{1/2} \right\}$$

$$Z = \dot{\epsilon} \exp \left(\frac{592.724}{RT} \right)$$

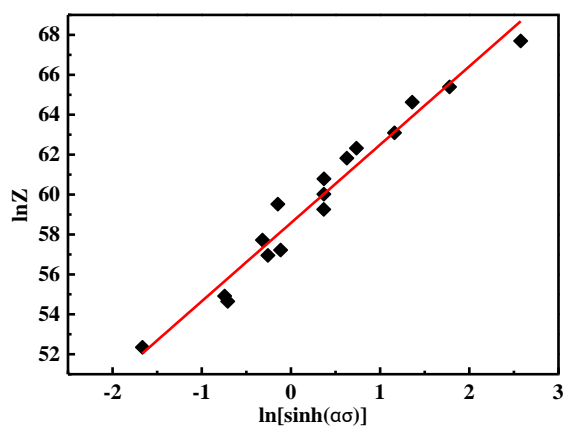
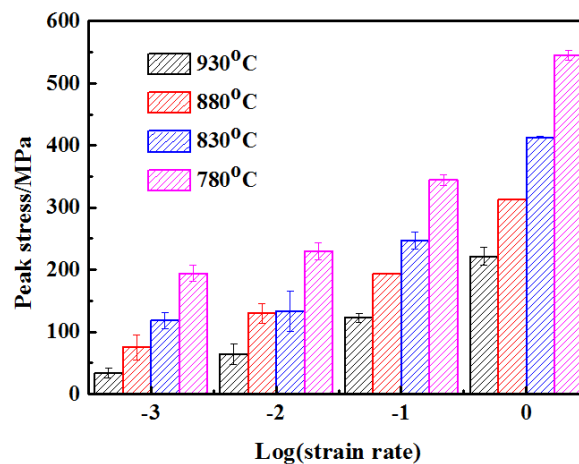


Figure 4. Plot of $\ln Z - \ln[\sinh(\alpha\sigma)]$.

Table 2. The calculated α , n , Q values for some typical near beta titanium alloys.

Material/Reference	α	n	Q (kJ/mol)
Ti-10V-2Fe-3Al [23]	0.011	2.51	534.0
Ti-5Al-5Mo-5V-3Cr-1Zr [24]	0.009	3.50	275.3
Ti-7333 [21]	0.007	4.13	333.7
Ti-4Al-1Sn-2Zr-5Mo-8V-2.5Cr (this work)	0.006	3.92	592.7

The peak flow stress under various deformation conditions is presented in Figure 5. The error bar in Figure 5 indicates the variations of experimental values while the height of the vertical bar indicates the predicted value from the above constitutive equation. It is clear that the constitutive equation fits experiments very well.

**Figure 5.** Peak flow stress under different deformation conditions.

3.2. Processing Map

Generally, a processing map based on dynamic materials model (DMM) is employed to analyze the ability of hot deformation for a particular alloy [25,26]. In DMM, the power dissipation efficiency η , which is associated with the work of hot deformation, can be described by the strain rate sensitivity m as [27]:

$$m = \frac{\varepsilon \partial \sigma}{\sigma \partial \varepsilon} \quad (5)$$

$$\eta = \frac{2m}{1+m} \quad (6)$$

The power dissipation map represents the manner in which the power is dissipated by the material through microstructure evolution [17]. Figure 6 shows the power dissipation map of the Ti-4Al-1Sn-2Zr-5Mo-8V-2.5Cr alloy for a strain of 0.7, which is constructed at strain rates ranging from 0.001 to 1 s⁻¹ and deformation temperature from 780 °C to 930 °C. It is clear that the variation of values of η is very sensitive to the deformation parameters (strain rate and deformation temperature). As shown in Figure 6, there are three distinct domains of peak efficiency. The first one occurs at the temperature range of 780 °C to 800 °C (in the $\alpha + \beta$ field), in which up to 50% of peak efficiency was observed at ~780 °C and 0.03 s⁻¹. The reason for the high efficiency of power dissipation in this region is likely the significant α to β transformation, globularization of α lamellae and dynamic recrystallization (DRX) [28]. The second domain appears in the single β field (temperature: 880 °C to 900 °C) and at the strain rate range of 0.3 to 1 s⁻¹. It presents a peak efficiency of 50% at ~880 °C and 0.1 s⁻¹, which implies the desired deformation mechanism could be achieved at high strain rates.

The third peak efficiency domain appears at temperatures from 900 °C to 930 °C with strain rate of 0.001 s⁻¹ to 0.01 s⁻¹; a peak efficiency of 60% was observed at about 930 °C and 0.001 s⁻¹. The high efficiency at these two domains is likely to be dominated by DRV and DRX [21].

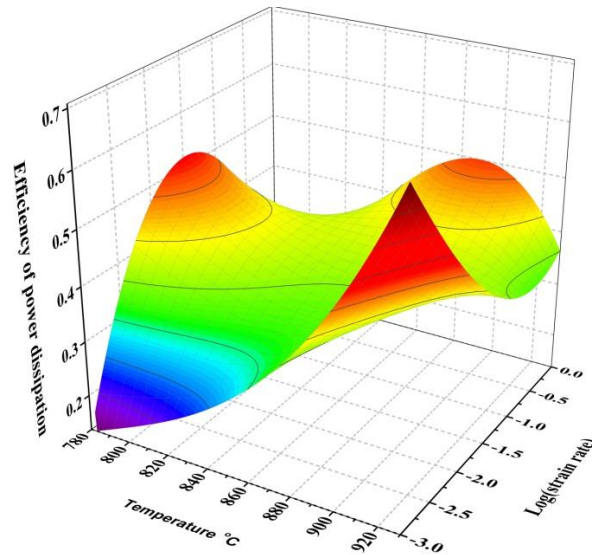


Figure 6. Power dissipation map of the current alloy at strain of 0.7.

The instability map is established according to the irreversible thermodynamics extremum principles used for the large-scale plastic deformation body. The instability criterion is described by the instability parameter ξ [29]:

$$\xi(\dot{\epsilon}) = \frac{\partial \ln\left(\frac{m}{m+1}\right)}{\partial \ln(\dot{\epsilon})} + m < 0 \quad (7)$$

The processing map can be superimposed by power dissipation map and instability map [18]. Processing map of the current alloy at a strain of 0.7 is presented in Figure 7. The contours represent the efficiency of power dissipation. The red shaded region represents the instability region, in which the values of instability parameter ξ , are negative. As shown in Figure 7, the Ti-4Al-1Sn-2Zr-5Mo-8V-2.5Cr alloy presents a wider process window in comparison with the other titanium alloys, which confirms the excellent workability of this material [13,18,30]. Previous investigations [30,31] suggest that the microstructural evolution in the stable domains is probably caused by DRX, spheroidizing or DRV. On the other hand, adiabatic shear bands formation, flow localization or flow rotations is likely the cause of flow instability.

To understand the deformation mechanisms of the Ti-4Al-1Sn-2Zr-5Mo-8V-2.5Cr alloy in different regions on the processing map, the microstructures of the deformed alloy under various processing conditions are analyzed and discussed in the following section.

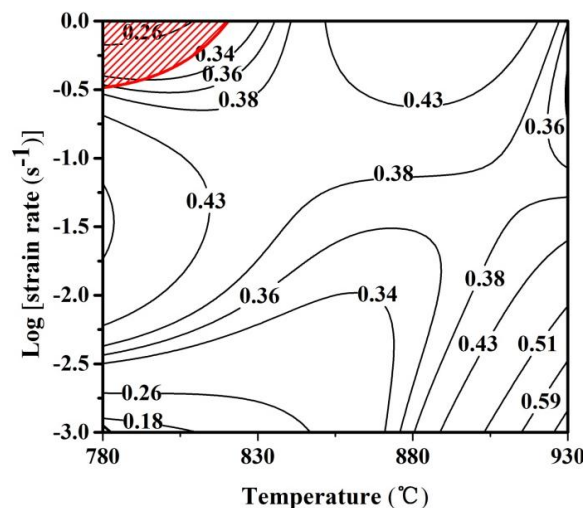


Figure 7. Processing map of the current alloy at strain of 0.7.

3.3. Microstructure

3.3.1. Samples Deformed in Flow Stability Regions

Typical microstructures of Ti-4Al-1Sn-2Zr-5Mo-8V-2.5Cr alloy in the stability regions of processing map are presented in Figure 8. As can be seen in Figure 8a, the coarser grains are obtained when compressed at 780 °C/0.001 s⁻¹, where the value of η is approximately 10%. The reasons for this phenomenon may be that sufficient impetus leads to finished dynamic recrystallization of β grains. Due to the high temperature in the $\alpha + \beta$ field and low strain rates, the sufficient power and time lead to completed dynamic recrystallization when strain is less than 0.7. It is also noted that precipitation of α phase is beneficial to the achievement of DRX [23]. The Q and η values under this condition are 477.2 kJ/mol and 10% respectively. With increasing the deformation temperature and strain rate, fine recrystallized grains are developed fully at 830 °C/0.01 s⁻¹, as observed in Figure 8b. Under this particular condition, the values of Q and η are 715.2 kJ/mol and 40%. It is consistent with other studies, in which dynamic recrystallization is achieved when the value of efficiency dissipation is in the range of 40–50% [32]. When deformed at 930 °C/0.1 s⁻¹, some sub grains (low angle grain boundaries) are presented in Figure 8c, suggesting dominant dynamic recovery (DRV) and only few recrystallized grains are observed along the boundaries. The dominance of DRV over DRX is likely due to the high stacking fault energy of β phase [21]. The corresponding values of Q and η are 403.3 kJ/mol and 36%. Decreasing strain rate and hence more sufficient time available promotes DRX; thus more recrystallized grains are developed, as shown in Figure 8d. The corresponding values of Q and η are 462.5 kJ/mol and 40%, respectively.

The above results indicate that the hot deformation at a proper deformation temperature and low strain rate could promote finer and homogeneous microstructure. The optimal hot working parameters for the current alloy are determined as temperature of 780 °C to 880 °C and strain rate of 0.001 to 0.01 s⁻¹.

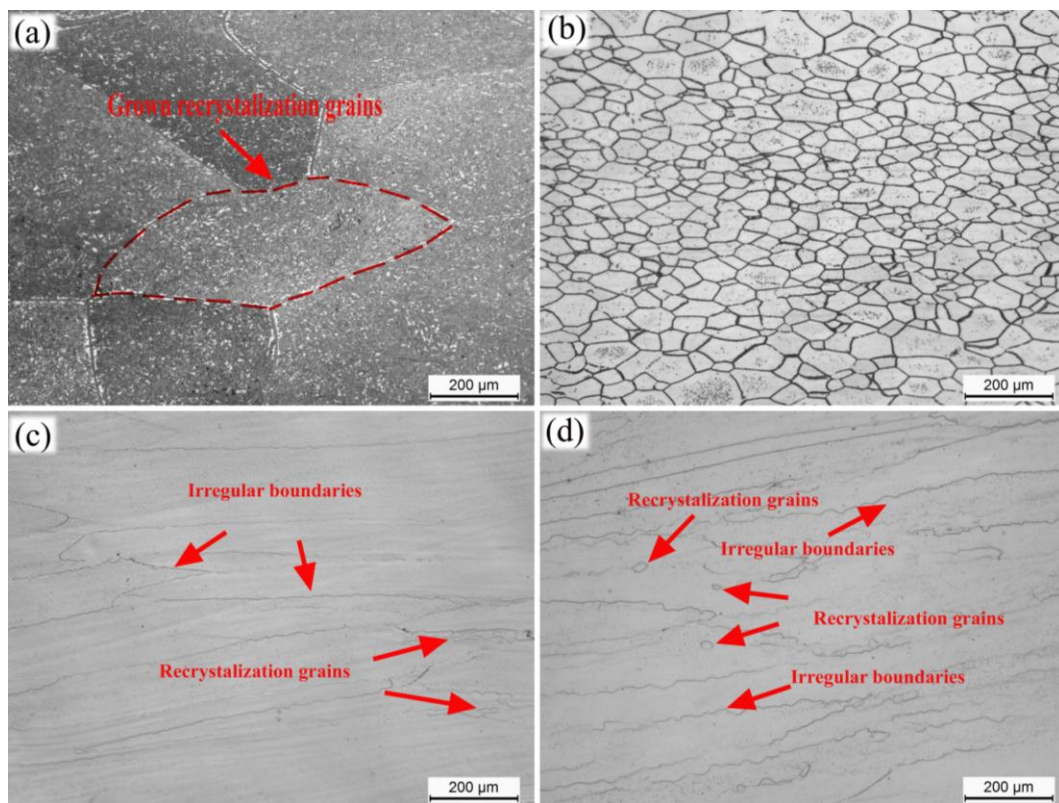


Figure 8. Microstructures of samples processed with different parameters (a) 780 °C/0.001 s⁻¹; (b) 830 °C/0.01 s⁻¹; (c) 930 °C/0.1 s⁻¹; and (d) 930 °C/0.01 s⁻¹.

3.3.2. Samples Deformed in Flow Instability Regions

The microstructures of the sample processed in the instability domains are presented in Figure 9. In general, the microstructure features the bands of flow localization, in association with localized flow or adiabatic shear bands [33,34]. The adiabatic heat is generated easily because Ti possesses a much lower thermal conductivity when compared to other metals [21]. By comparing the microstructure in Figure 9a,b, the bands of flow localization are more obvious at higher strain rates. This is caused by an increased accumulated energy at a high strain rate. In addition to strain rate, deformation temperature apparently influences the microstructure. It is expected that, for a given high strain rate, further decreasing deformation temperature would result in cracking (not presented in this study). Meanwhile, the SEM micrograph of the current alloy is presented in Figure 10, which shows a fairly heterogeneous microstructure. The majority are fine elongated α lamella perpendicular to the compression axis. There exist some irregularly bent α lamella as well. In terms of processing safety, the deformation parameters in the top left corner of Figure 7 (i.e., instability domain) is not recommended for the processing of the Ti-4Al-1Sn-2Zr-5Mo-8V-2.5Cr alloy.

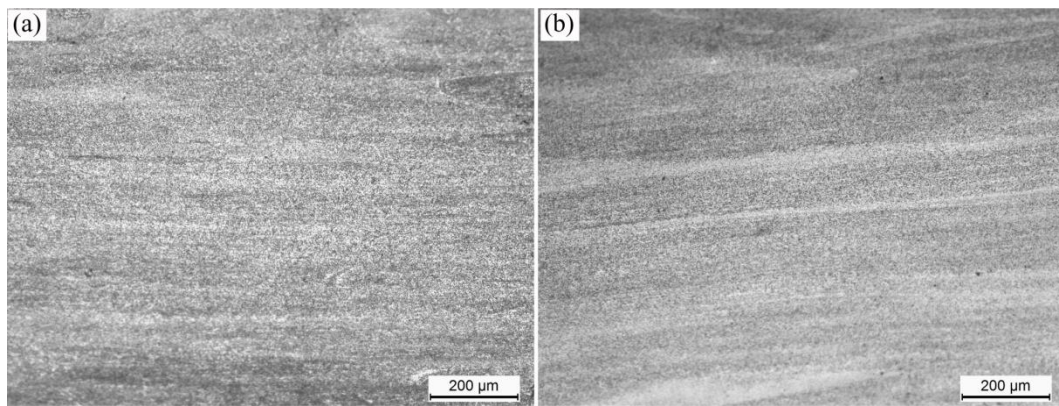


Figure 9. Microstructure observed in specimens deformed in the instability regions (a) 780 °C, 0.1 s⁻¹ and (b) 780 °C, 1 s⁻¹.

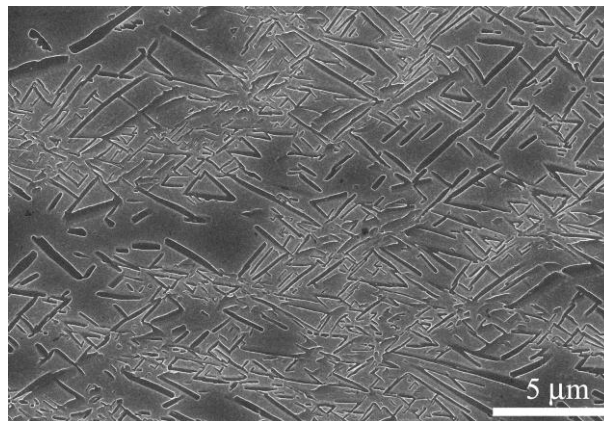


Figure 10. Scanning Electron Microscopy (SEM) micrograph of α lamellae deformed at 780 °C, 1 s⁻¹.

4. Conclusions

This study investigated the hot deformation behavior of a newly developed near β titanium alloy, Ti-4Al-1Sn-2Zr-5Mo-8V-2.5Cr. Based on the results obtained from the hot compression tests, a constitutive model and processing maps are developed. Additionally the microstructures under various processing conditions are observed to verify the deformation mechanisms. The following conclusions can be drawn from the present study:

1. The flow stress variation of Ti-4Al-1Sn-2Zr-5Mo-8V-2.5Cr alloy is strongly dependent on the strain rate and deformation temperature. The peak flow stress decreases with decreasing strain rate and increasing temperature.
2. The constitutive equation is constructed and the average deformation activation energy is calculated to be 592.7 kJ/mol. The constitutive equations for the current alloy are:

$$Z = \dot{\epsilon} \exp\left(\frac{592724}{RT}\right)$$

$$\sigma = 166.67 \ln \left\{ \left(\frac{Z}{e^{58.58}} \right)^{1/3.92} + \left[\left(\frac{Z}{e^{58.58}} \right)^{2/3.92} + 1 \right]^{1/2} \right\}$$

3. The dominant mechanism in the instability domain is the flow localizations, while in the stability domains, the mechanisms are DRV and DRX. The optimal processing parameters are obtained in the temperature range of 780 °C to 880 °C and strain rate of 0.001 to 0.01 s⁻¹.

Acknowledgments: The authors gratefully thank the financial support from the National Natural Science Foundation of China (No. 51504163 and 51604191).

Author Contributions: All authors have contributed significantly. Changjiang Zhang, Peng Cao and Jie Wu designed the project. Zhidan Lü, Jianchao Han, Hongzhou Zhang, Shuzhi Zhang undertook the experiments and data collection. Jie Wu, Zhidan Lü, Changjiang Zhang and Muhammad Hayat analyzed the data. All authors contributed to the discussion of the results. Jie We, Changjiang Zhang and Peng Cao wrote and revised the manuscript.

Conflicts of Interest: The authors declare no conflict of interest.

References

1. Zhang, X.E.; Zhang, J.S.; Chen, F.; Yang, Z.J.; He, J.L. Characteristics of resistance spot welded Ti₆Al₄V titanium alloy sheets. *Metals* **2017**, *10*, 424. [[CrossRef](#)]
2. Zhang, Q.; Chen, J.; Wang, L.; Tan, H.; Lin, X.; Huang, W. Solidification microstructure of laser additive manufactured Ti-6Al-2Zr-2Sn-3Mo-1.5Cr-2Nb titanium alloy. *J. Mater. Sci. Technol.* **2016**, *32*, 381–386. [[CrossRef](#)]
3. Zhao, Z.; Chen, J.; Guo, S.; Tan, H.; Lin, X.; Huang, W. Influence of α/β interface phase on the tensile properties of laser cladding deposited Ti-6Al-4V titanium alloy. *J. Mater. Sci. Technol.* **2017**, *33*, 675–681. [[CrossRef](#)]
4. Tang, B.; Kou, H.; Zhang, X.; Gao, P.; Li, J. Study on the formation mechanism of α lamellae in a near β titanium alloy. *Prog. Nat. Sci. Mater. Inter.* **2016**, *26*, 385–390. [[CrossRef](#)]
5. Du, Z.X.; Xiao, S.L.; Shen, Y.P.; Liu, J.S.; Liu, J.; Xu, L.J.; Kong, F.T.; Chen, Y.Y. Effect of hot rolling and heat treatment on microstructure and tensile properties of high strength beta titanium alloy sheets. *Mater. Sci. Eng. A* **2015**, *631*, 67–74. [[CrossRef](#)]
6. Boyer, R.R. An overview on the use of titanium in the aerospace industry. *Mater. Sci. Eng. A* **1996**, *213*, 103–114. [[CrossRef](#)]
7. Bruschi, S.; Buffa, G.; Ducato, A.; Fratini, L.; Ghiotti, A. Phase evolution in hot forging of dual phase titanium alloys: Experiments and numerical analysis. *J. Manuf. Process.* **2015**, *20*, 382–388. [[CrossRef](#)]
8. Guo, L.; Fan, X.; Yu, G.; Yang, H. Microstructure control techniques in primary hot working of titanium alloy bars: A review. *Chin. J. Aeronaut.* **2016**, *29*, 30–40. [[CrossRef](#)]
9. Weiss, I.; Semiatin, S.L. Thermomechanical processing of beta titanium alloys—An overview. *Mater. Sci. Eng. A* **1998**, *243*, 46–65. [[CrossRef](#)]
10. Zhou, Y.G.; Zeng, W.D.; Yu, H.Q. An investigation of a new near-beta forging process for titanium alloys and its application in aviation components. *Mater. Sci. Eng. A* **2005**, *393*, 204–212. [[CrossRef](#)]
11. Carrino, L.; Paradiso, V.; Franchitti, S.; Squillace, A.; Russo, S. Superplastic forming/diffusion bonding of a titanium alloy for the realization of an aircraft structural component in multi-sheets configuration. *Key Eng. Mater.* **2012**, *504–506*, 712–722. [[CrossRef](#)]
12. Wang, K.; Lu, S.; Fu, M.W.; Li, X.; Dong, X. Optimization of β /near- β forging process parameters of Ti-6.5Al-3.5Mo-1.5Zr-0.3Si by using processing maps. *Mater. Charact.* **2009**, *60*, 492–498. [[CrossRef](#)]
13. Wang, Z.; Wang, X.; Zhu, Z. Characterization of high-temperature deformation behavior and processing map of TB17 titanium alloy. *J. Alloys Compd.* **2017**, *692*, 149–154. [[CrossRef](#)]
14. Zhao, J.; Zhong, J.; Yan, F.; Chai, F.; Dargusch, M. Deformation behaviour and mechanisms during hot compression at supertransus temperatures in Ti-10V-2Fe-3Al. *J. Alloys Compd.* **2017**, *710*, 616–627. [[CrossRef](#)]
15. Zhao, H.Z.; Xiao, L.; Ge, P.; Sun, J.; Xi, Z.P. Hot deformation behavior and processing maps of Ti-1300 alloy. *Mater. Sci. Eng. A* **2014**, *604*, 111–116. [[CrossRef](#)]
16. Li, J.; Liu, Y.; Liu, B.; Wang, Y.; Cao, P.; Zhou, C.; Xiang, C.; He, Y. High temperature deformation behavior of near γ -phase high Nb-containing TiAl alloy. *Intermetallics* **2014**, *52*, 49–56. [[CrossRef](#)]
17. Zhu, Y.; Zeng, W.; Feng, F.; Sun, Y.; Han, Y.; Zhou, Y. Characterization of hot deformation behavior of as-cast TC21 titanium alloy using processing map. *Mater. Sci. Eng. A* **2011**, *528*, 1757–1763. [[CrossRef](#)]

18. Li, L.; Li, M. Constitutive model and optimal processing parameters of TC17 alloy with a transformed microstructure via kinetic analysis and processing maps. *Mater. Sci. Eng. A* **2017**, *698*, 302–312. [[CrossRef](#)]
19. Liu, D.; Liu, Y.; Zhao, Y.; Huang, Y.; Chen, M. The hot deformation behavior and microstructure evolution of HA/Mg-3Zn-0.8Zr composites for biomedical application. *Mater. Sci. Eng. C* **2017**, *77*, 690–697. [[CrossRef](#)] [[PubMed](#)]
20. Haghdadadi, N.; Zarei-Hanzaki, A.; Khalesian, A.R.; Abedi, H.R. Artificial neural network modeling to predict the hot deformation behavior of an A356 aluminum alloy. *Mater. Des.* **2013**, *49*, 386–391. [[CrossRef](#)]
21. Fan, J.K.; Kou, H.C.; Lai, M.J.; Tang, B.; Chang, H.; Li, J.S. Characterization of hot deformation behavior of a new near beta titanium alloy: Ti-7333. *Mater. Des.* **2013**, *49*, 945–952. [[CrossRef](#)]
22. Flower, H.M. Microstructural development in relation to hot working of titanium alloys. *Mater. Sci. Technol.* **1990**, *6*, 1082–1092. [[CrossRef](#)]
23. Ravindranadh, B.; Venkata, R.B.; Madhu, V. A physically-based constitutive model for hot deformation of Ti-10-2-3 alloy. *J. Alloys Compd.* **2017**, *696*, 295–303.
24. Warchomicka, F.; Poletti, C.; Stockinger, M. Study of the hot deformation behaviour in Ti-5Al-5Mo-5V-3Cr-1Zr. *Mater. Sci. Eng. A* **2011**, *528*, 8277–8285. [[CrossRef](#)]
25. Guo, S.; Li, D.; Wu, X.; Xu, X.; Du, P.; Hu, J. Characterization of hot deformation behavior of a Zn-10.2Al-2.1Cu alloy using processing maps. *Mater. Des.* **2012**, *41*, 158–166. [[CrossRef](#)]
26. Zhou, Z.; Fan, Q.; Xia, Z.; Hao, A.; Yang, W.; Ji, W.; Cao, H. Constitutive Relationship and Hot Processing Maps of Mg-Gd-Y-Nb-Zr Alloy. *J. Mater. Process. Technol.* **2017**, *33*, 637–644. [[CrossRef](#)]
27. Basanth, K.K.; Saxena, K.K.; Dey, S.R.; Pancholi, V.; Bhattacharjee, A. Processing map-microstructure evolution correlation of hot compressed near alpha titanium alloy (TiHy 600). *J. Alloys Compd.* **2017**, *691*, 906–913.
28. Prasad, Y.V.R.K.; Seshacharyulu, T. Processing maps for hot working of titanium alloys. *Mater. Sci. Eng. A* **1998**, *243*, 82–88. [[CrossRef](#)]
29. Luo, J.; Li, M.; Yu, W.; Li, H. Effect of the strain on processing maps of titanium alloys in isothermal compression. *Mater. Sci. Eng. A* **2009**, *504*, 90–98. [[CrossRef](#)]
30. Peng, X.; Guo, H.; Shi, Z.; Qin, C.; Zhao, Z.; Yao, Z. Study on the hot deformation behavior of TC4-DT alloy with equiaxed $\alpha + \beta$ starting structure based on processing map. *Mater. Sci. Eng. A* **2014**, *605*, 80–88. [[CrossRef](#)]
31. Sun, Y.; Zeng, W.D.; Zhao, Y.Q.; Zhang, X.M.; Shu, Y.; Zhou, Y.G. Research on the hot deformation behavior of Ti40 alloy using processing map. *Mater. Sci. Eng. A* **2011**, *528*, 1205–1211. [[CrossRef](#)]
32. Matsumoto, H.; Kitamura, M.; Li, Y.; Koizumi, Y.; Chiba, A. Hot forging characteristic of Ti-5Al-5V-5Mo-3Cr alloy with single metastable. *Mater. Sci. Eng. A* **2014**, *611*, 337–344. [[CrossRef](#)]
33. Zong, Y.Y.; Shan, D.B.; Xu, M.; Lv, Y. Flow softening and microstructural evolution of TC11 titanium alloy during hot deformation. *J. Mater. Process. Technol.* **2009**, *209*, 1988–1994. [[CrossRef](#)]
34. Momeni, A.; Abbasi, S.M. Effect of hot working on flow behavior of Ti-6Al-4V alloy in single phase and two phase regions. *Mater. Des.* **2010**, *31*, 3599–3604. [[CrossRef](#)]

